Filtering Reaction Dynamics Using Nearside−Farside Theory and Local Angular Momentum Theory: Application to the Angular Scattering of the H + $D_2(v_i = 0, j_i = 0) \rightarrow HD(v_f = 3, j_f = 0)$ + D Reaction in the Energy and Time Domains†

P. D. D. Monks and J. N. L. Connor*

School of Chemistry, The University of Manchester, Manchester M13 9PL, England

F. Bouakline

Department of Chemistry, University of Cambridge, Lensfield Road, Cambridge CB2 1EW, England

Received: January 19, 2009; Revised Manuscript Received: February 16, 2009

We investigate methods for filtering reaction mechanisms in the angular scattering of the state-to-state reaction, $H + D_2(v_i = 0, j_i = 0, m_i = 0) \rightarrow HD(v_f = 3, j_f = 0, m_f = 0) + D$, where v_i, j_i, and m_i and v_f, j_f, and m_f are initial and final vibrational, rotational, and helicity quantum numbers, respectively. The input to our filtrations is a new set of accurate quantum scattering matrix elements for total energies in the range 1.52−2.50 eV (in steps of 0.01 eV) and for total angular momentum quantum numbers in the range, 0−40, in steps of unity. We filter reaction mechanisms in both the energy domain and the time domain. The time-domain calculations employ the plane wave packet formulation of time-dependent scattering. The theoretical tools used are nearside−farside (NF) analysis of partial wave series for scattering amplitudes, together with NF local angular momentum (LAM) theory. An energy-domain LAM analysis reveals the existence of an important dynamical feature in the N scattering, a "trench" which bisects the (energy, angle) plane. We use the location of this trench to approximately filter two reaction mechanisms. Transformation to the time domain demonstrates that the two reaction mechanisms correspond to direct and delayed (by about 25 fs) scattering. Further analysis, including filtration in the time domain, shows that the pronounced LAM trench arises from the interference of the energy-domain analogues of the time-direct and time-delayed scattering. Our theory and results provide the first successful demonstration of reaction mechanism filtering carried out directly in the (energy, angle) domain. The calculations and results in this paper extend and complement earlier research reported by Monks, Connor, and Althorpe (Monks, P. D. D.; Connor, J. N. L.; Althorpe, S. C. *J. Phys. Chem. A* **2006**, *110*, 741; *J. Phys. Chem. A* **2007**, *111*, 10302).

1. Introduction

This paper is the third in a series[1,2] using nearside−farside (NF) theory and local angular momentum (LAM) theory to understand the dynamics of the state-to-state reaction

$$H + D_2(v_i = 0, j_i = 0, m_i = 0) \rightarrow HD(v_f = 3, j_f = 0, m_f = 0) + D$$

where v_i, j_i, and m_i and v_f, j_f, and m_f are vibrational, rotational, and helicity quantum numbers for the initial and final states, respectively. We are studying the H + D_2 collision system because it is a benchmark reaction[1−13] that exhibits interesting scattering dynamics. It has been extensively researched in experiments and by theory during the past few years.[1,2,12−22]

In our first paper,[1] we studied the *time-dependent* dynamics of the H + D_2 reaction because it has the interesting property that two reaction mechanisms are present: one time direct, the other time delayed (by about 25 fs). The theoretical techniques used in ref 1 were a general *Plane Wave Packet* (*PWP*) theory of molecular scattering[1,23−32] (reviewed in refs 30 and 31), together with a NF decomposition[1,2,33−57] (reviewed in refs 11 and 57−59) of the time dependent scattering amplitude. Other recent applications of NF theory are given in refs 15, 16, and 60−76. We also used the related NF concept of a LAM.[1,2,49,50,52,55−57,68] In addition, ref 1 introduced the novel concepts of a cumulative time-evolving differential cross section and a cumulative energy-evolving angular distribution.

Our second paper[2] reported NF and LAM analyses of the *time-independent* (energy-domain) scattering amplitude over a range of total energies. We also resummed the partial wave series for the scattering amplitude up to three times before making the NF decomposition and showed that such resummations usually provide an improved physical understanding of the NF differential cross sections.

The purpose of this paper is to extend the work in refs 1 and 2 in a different direction by using NF and LAM theory to *filter reaction mechanisms* in the angular scattering of the H + D_2 reaction. The quantum filtration procedure proposed in refs 23−26, and 32 is the following: The PWP angular distribution in the time-domain is examined and in favorable cases two reaction mechanisms may be seen, e.g., direct and delayed scattering. These mechanisms can be approximately separated with the help of filters defined by a curve which cuts the (time, angle) plane. An (inverse-) Fourier transformation of the separate (filtered) mechanisms into the energy domain then allows the analogues of the two time-domain mechanisms to be identified and studied in the (energy, angle) plane. This filtration procedure has been applied to the H + $D_2 \rightarrow$ HD + D,[23,24] F + HD → FH

† Part of the "George C. Schatz Festschrift".

10.1021/jp9005586 CCC: $40.75
Published on Web 03/27/2009

+ D,[25,26] and He + $H_2^+ \rightarrow HeH^+ + H$ reactions.[32] The last reaction[32] also combined filtering with a simple asymptotic version of NF theory.[43]

In this paper, we show that the analogues of the direct and delayed mechanisms can be identified directly in the energy domain, without first going into the time domain. This is possible because an energy-domain LAM analysis reveals the existence of an important dynamical feature in the N scattering: a "trench" which bisects the (energy, angle) plane. We use the location of this trench to design a filter that approximately separates the two reaction mechanisms. Fourier transformation to the time domain confirms that the two reaction mechanisms indeed correspond to direct and delayed scattering.

Section 2 describes the necessary NF and LAM theories needed for our computations in the energy and time domains. We also discuss how to obtain filtered time-domain subamplitudes from the bisected energy-domain scattering amplitude (and vice versa).

The input to our calculations is a new set of accurate quantum scattering matrix elements for total energies in the range 1.52−2.50 eV (in steps of 0.01 eV) and for total angular momentum quantum numbers in the range 0−40, in steps of unity.[19] Note that we measure the total energy with respect to the asymptotic energy of the system where D_2 is at its equilibrium geometry in its ground electronic state and H is at an infinite distance from D_2 (i.e., the total energy is measured from the classical minimum of the D_2 potential energy curve). The computations for the scattering matrix are briefly described in section 3, together with the filters that we use to approximately separate the reaction mechanisms.

Our results are presented in section 4. We first examine the full and NF differential cross sections and LAMs in the energy domain. Second, we Fourier transform to the time domain, where we introduce filters and a cut curve which bisects the (time, angle) plane. Third, we make a detailed study in the energy domain of the analogues of the time-direct and time-delayed mechanisms and show that the LAM trench arises from the interference of these two mechanisms. Our conclusions are in section 5.

This paper together with refs 1 and 2 use a consistent set of notations and conventions. In particular, throughout the present paper, we use the notation $w = x(y)z$ to mean increment w in steps of y, starting from $w = x$ and finishing at $w = z$.

2. Theoretical Methods

A. Energy-Domain Scattering Amplitude, Nearside−Farside Decomposition and Local Angular Momentum. We begin with the energy-domain scattering amplitude, $f(\theta_R,E)$, where E is the total energy and θ_R is the reactive scattering angle, i.e., the angle between the outgoing HD molecule and the incoming H atom. We can expand $f(\theta_R,E)$ in a basis set of Legendre polynomials, since the initial and final helicity quantum numbers are both zero for the present state-to-state reaction. We write for the partial wave series (PWS)

$$f(\theta_R, E) = \frac{1}{2ik(E)} \sum_{J=0}^{\infty} (2J + 1)\tilde{S}_J(E)P_J(\cos\theta_R) \qquad (1)$$

where $k(E)$ is the initial translational wavenumber, J is the total angular momentum quantum number, $\tilde{S}_J(E)$ is a modified energy-dependent scattering matrix element, and $P_J(\bullet)$ is a Legendre polynomial of degree J. Note that initial- and final-state labels have been omitted from eq 1, and in the following, for simplicity of notation. The corresponding differential cross section (DCS) is given by

$$\sigma(\theta_R, E) = |f(\theta_R, E)|^2 \qquad (2)$$

We next decompose $f(\theta_R,E)$ into the sum of two subamplitudes using the Fuller NF procedure[77]

$$f(\theta_R, E) = f_N(\theta_R, E) + f_F(\theta_R, E) \qquad (3)$$

where the N and F subamplitudes are, for $\theta_R \neq 0,\pi$

$$f_{N,F}(\theta_R, E) = \frac{1}{2ik(E)} \sum_{J=0}^{\infty} (2J + 1)\tilde{S}_J(E)Q_J^{(\mp)}(\cos\theta_R) \qquad (4)$$

with $Q_J^{(\mp)}(\bullet)$ defined by the linear combinations ($\theta_R \neq 0,\pi$)

$$Q_J^{(\mp)}(\cos\theta_R) = \frac{1}{2}\left[P_J(\cos\theta_R) \pm \frac{2i}{\pi}Q_J(\cos\theta_R)\right] \qquad (5)$$

and $Q_J(\bullet)$ is a Legendre function of the second kind of degree J. The corresponding NF DCSs are obtained from ($\theta_R \neq 0,\pi$)

$$\sigma_{N,F}(\theta_R, E) = |f_{N,F}(\theta_R, E)|^2 \qquad (6)$$

In many cases, graphs of $\sigma(\theta_R,E)$ display complicated behavior when plotted against θ_R (at fixed E). In this situation, plots of $\sigma_{N,F}(\theta_R,E)$ versus θ_R often exhibit simpler behavior, which can help us understand the dynamics of the reaction. In particular, we can interpret structure in a plot of $\sigma(\theta_R,E)$ versus θ_R as arising from the N contribution to $f(\theta_R E)$ or from the F contribution or from interference between the N and F subamplitudes.

The local angular momentum is defined by the equation[49,50,52]

$$\mathrm{LAM}(\theta_R, E) = \frac{\partial \arg f(\theta_R, E)}{\partial\theta_R} \qquad (7)$$

where the arg is not necessarily the principal value in order that the derivative be well-defined. LAM is measured in units of $\hbar$; in the semiclassical limit, it contains information on the total angular momentum that contributes to the scattering at the angle θ_R. The LAM is a real (positive or negative) number and is not confined to integer values. Positive values of $\mathrm{LAM}(\theta_R,E)$ result from the anticlockwise motion of $\arg f(\theta_R,E)$ as θ_R increases and usually correspond to attractive forces. Similarly, negative values result from the clockwise motion of $\arg f(\theta_R,E)$ as θ_R increases, which usually correspond to repulsive forces. These two types of behavior are usually attributable to F and N contributions, respectively.

N and F LAMs can also be defined and are given by[49,50,52]

$$\mathrm{LAM}_{N,F}(\theta_R, E) = \frac{\partial \arg f_{N,F}(\theta_R, E)}{\partial\theta_R} \qquad (8)$$

B. Time-Domain Scattering Amplitude and Nearside−Farside Decomposition. This section presents the equations from the PWP theory of time-dependent scattering needed for

our calculations in section 3. We define a time-dependent scattering amplitude, $f(\theta_R,t)$, where t is the time, by the half-Fourier transform[1,28,29]

$$f(\theta_R, t) = \int_0^\infty F(E) f(\theta_R, E) \exp(-iEt/\hbar)\, dE \qquad (9)$$

$$\text{n.b., dimensions} = \text{length} \times \text{energy}$$

In eq 9, $F(E)$ is a dimensionless complex-valued energy filter function,[1,28,29] which is chosen to extract interesting information from $f(\theta_R,E)$ and map it to the time domain as described by $f(\theta_R,t)$. We use a filter function in section 3 that has the property $F(E) \rightarrow 0$ as $E \rightarrow \infty$. Note that ref 26 has introduced a more general filter which also depends on J.

We choose $t = 0$ in the integral (9) as a time before H and D_2 have interacted. We can then assume $f(\theta_R,t) \equiv 0$ for $t < 0$. As $t \rightarrow \infty$ we will have $f(\theta_R,t) \rightarrow 0$ by the Riemann−Lebesgue Lemma because the exponential factor in the integrand of eq 9 will oscillate faster and faster (assuming $F(E)$ and $f(\theta_R,E)$ are well behaved). Thus $f(\theta_R,t)$ will only be significantly different from zero for $0 < t < t_{max}$, where t_{max} is a time at which the reaction is over and HD and D are no longer interacting.

We also define

$$\sigma(\theta_R, t) = |f(\theta_R, t)|^2 \qquad (10)$$

by analogy with the DCS, eq 2. We will call $\sigma(\theta_R,t)$ a "time-dependent angular distribution" or a "time-dependent scattering pattern" rather than a "time-dependent differential cross section" since $\sigma(\theta_R,t)$ has dimensions of length^2 × energy^2 rather than length^2.

The inverse Fourier transform of eq 9 is

$$f(\theta_R, E) = \frac{1}{2\pi\hbar F(E)} \int_0^\infty f(\theta_R, t) \exp(iEt/\hbar)\, dt \qquad (11)$$

$$\text{n.b., dimensions} = \text{length}$$

Notice that we employ the same symbol f for the different functions $f(\theta_R,E)$ and $f(\theta_R,t)$ and use their differing arguments to distinguish them. This convention is also adopted for other physical quantities in the energy and time domains in order to keep the notation simple.

We can make a partial wave expansion for $f(\theta_R,t)$ by writing[1,28,29]

$$f(\theta_R, t) = \frac{1}{2i} \sum_{J=0}^{\infty} (2J+1) \tilde{S}_J(t) P_J(\cos\theta_R) \qquad (12)$$

where $\tilde{S}_J(t)$ is a modified time-dependent scattering matrix element. Substituting eqs 1 and 12 into eq 9 leads to

$$\tilde{S}_J(t) = \int_0^\infty \frac{F(E)}{k(E)} \tilde{S}_J(E) \exp(-iEt/\hbar)\, dE \qquad (13)$$

$$\text{n.b, dimensions} = \text{length} \times \text{energy}$$

The inverse Fourier transformation of eq 13 is

$$\tilde{S}_J(E) = \frac{1}{2\pi\hbar} \frac{k(E)}{F(E)} \int_0^\infty \tilde{S}_J(t) \exp(iEt/\hbar)\, dt \qquad (14)$$

We can also make a NF decomposition of $f(\theta_R,t)$ in order to better understand structure seen in $\sigma(\theta_R,t)$ when it is plotted versus θ_R at fixed values of t. By analogy with eqs 3−6, the NF decomposition of $f(\theta_R,t)$ is written[1]

$$f(\theta_R, t) = f_N(\theta_R, t) + f_F(\theta_R, t) \qquad (15)$$

where the NF time-dependent subamplitudes are ($\theta_R \neq 0,\pi$)

$$f_{N,F}(\theta_R, t) = \frac{1}{2i} \sum_{J=0}^{\infty} (2J+1) \tilde{S}_J(t) Q_J^{(\mp)}(\cos\theta_R) \qquad (16)$$

and the corresponding NF time-dependent angular distributions are ($\theta_R \neq 0,\pi$)

$$\sigma_{N,F}(\theta_R, t) = |f_{N,F}(\theta_R, t)|^2 \qquad (17)$$

In addition, we can also define full and N,F LAMs in the time domain[1] by analogy with eqs 7 and 8; however they are not used in the present paper.

C. Obtaining Filtered Time-Domain Subamplitudes from the Energy-Domain Scattering Amplitude. We begin by examining the properties of $\sigma(\theta_R,E)$ where E is the total energy. We show in Figure 1 a contour plot of $\sigma(\theta_R,E)$ using accurate quantum scattering matrix elements for the H + D_2 reaction with $0 \leq \theta_R/\text{deg} \leq 180$ and $1.52 \leq E/\text{eV} \leq 2.50$, where we have anticipated our results in section 4. We wish to cut the (θ_R,E) plane by a curve that approximately separates (filters) two reaction mechanisms, these being the energy-domain analogues of the time-direct and time-delayed mechanisms. Typically the direct mechanism arises from low impact parameter collisions in which H recoils backward after abstracting a D atom, while the delayed mechanism is mainly caused by larger impact parameter collisions which allow the HDD complex to rotate and decay into the forward direction. A possible cut-curve is drawn in red in Figure 1, where it is superimposed on the contour plot of $\sigma(\theta_R,E)$. We denote a cut-curve in the energy-domain by CC_E.

Our aim is to decompose $f(\theta_R,E)$ into the sum of two subamplitudes:

One for the energy-domain analogue of the time-direct scattering, denoted $f^{dir}(\theta_R,E)$, which will mainly lie to the right of CC_E in Figure 1.

One for the energy-domain analogue of the time-delayed scattering, denoted $f^{del}(\theta_R,E)$, which will mainly lie to the left of CC_E in Figure 1.

Remark: We could develop the theory using the more general labels "mechanism A" in place of "direct", and "mechanism B" in place of "delayed". However it is convenient to anticipate our results from section 4.

We can now make the decomposition

$$f(\theta_R, E) = f^{dir}(\theta_R, E) + f^{del}(\theta_R, E) \qquad (18)$$

We obtain the subamplitudes, $f^{dir,del}(\theta_R,E)$, by applying filter functions, $\xi^{dir,del}(\theta_R,E)$ to $f(\theta_R,E)$, which overlap on the cut-curve,

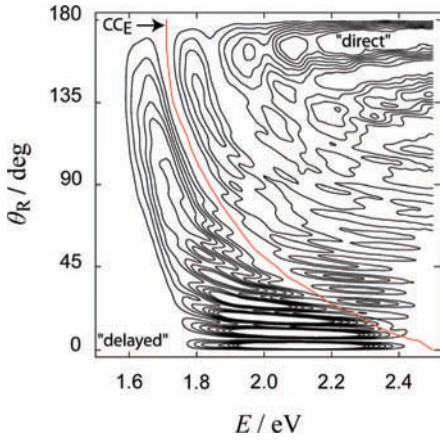

Figure 1. Contour plot of $\sigma(\theta_R,E)$. The values of the seven contours are 0.000025 (0.000025) 0.000175 Å^2 sr^{-1}. The red curve, called CC_E in the text, indicates the location of the center of the trench in the (θ_R,E) plane seen in Figures 5b and 6. CC_E is not a contour and approximately separates the energy-domain analogues of the time-direct and time-delayed scattering, which are denoted "direct" and "delayed", respectively.

together with a simple partition of unity, $\xi^{dir}(\theta_R,E) + \xi^{del}(\theta_R,E) = 1$. Specifically we have

$$f^{del}(\theta_R, E) = \xi^{del}(\theta_R, E) f(\theta_R, E) \tag{19}$$

and

$$f^{dir}(\theta_R, E) = \xi^{dir}(\theta_R, E) f(\theta_R, E) = [1 - \xi^{del}(\theta_R, E)] f(\theta_R, E) \tag{20}$$

The form of $\xi^{del}(\theta_R,E)$ is discussed in detail in section 3B, but its general properties at a fixed value of θ_R are $\xi^{del}(\theta_R,E) \rightarrow 1$ as $E \rightarrow E_{threshold}$ (the threshold energy for the stated-to-state reaction) and $\xi^{del}(\theta_R,E) \rightarrow 0$ as $E \rightarrow \infty$.

Next we operate with the half-Fourier transform of eq 9 on the $f^{dir,del}(\theta_R,E)$. The results of this operation are two filtered time-dependent subamplitudes, $f^{dir}(\theta_R,t)$ and $f^{del}(\theta_R,t)$, which approximately represent the time-direct and time-delayed mechanisms, respectively. They are defined by

$$f^{dir,del}(\theta_R, t) = \int_0^\infty F(E) f^{dir,del}(\theta_R, E) \exp(-iEt/\hbar)\, dE \tag{21}$$

The same operations described by eqs 18−21 can also be applied to the N and F subamplitudes $f_{N,F}(\theta_R,E)$, resulting in the sub-subamplitudes, ${f_{N,F}}^{dir}(\theta_R,t)$ and ${f_{N,F}}^{del}(\theta_R,t)$. In more detail

$${f_{N,F}}(\theta_R, E) = {f_{N,F}}^{dir}(\theta_R, E) + {f_{N,F}}^{del}(\theta_R, E) \tag{22}$$

and

$${f_{N,F}}^{dir,del}(\theta_R, t) = \int_0^\infty F(E) {f_{N,F}}^{dir,del}(\theta_R, E) \exp(-iEt/\hbar)\, dE \tag{23}$$

where the ${f_{N,F}}^{dir,del}(\theta_R,E)$ are defined by analogy with eqs 19 and 20, i.e.

$${f_{N,F}}^{del}(\theta_R, E) = \xi^{del}(\theta_R, E) f_{N,F}(\theta_R, E) \tag{24}$$

and

$${f_{N,F}}^{dir}(\theta_R, E) = \xi^{dir}(\theta_R, E) f_{N,F}(\theta_R, E) = [1 - \xi^{del}(\theta_R, E)] f_{N,F}(\theta_R, E) \tag{25}$$

Having defined the filtered time-dependent subamplitudes, $f^{dir,del}(\theta_R,t)$ by eq 21, we can calculate filtered time-dependent angular distributions by

$$\sigma^{dir,del}(\theta_R, t) = |f^{dir,del}(\theta_R, t)|^2 \tag{26}$$

We can also define NF filtered time-dependent angular distributions by

$$\sigma_{N,F}{}^{dir,del}(\theta_R, t) = |{f_{N,F}}^{dir,del}(\theta_R, t)|^2 \tag{27}$$

Some, or all, of these filtered time-dependent angular distributions may be used to help separate the time-direct and time-delayed mechanisms in the time domain. This approach allows us to remove some of the ambiguity for finding a boundary, or cut-curve, between the direct and delayed mechanisms in the time domain. Our results using this approach are described in section 4.

We will call the filtration described in this section as "CC_E filtering" for brevity.

D. Obtaining Filtered Energy-Domain Subamplitudes from the Time-Domain Scattering Amplitude. We now consider the reverse process to that described in section 2C. Suppose a suitable cut-curve has been found within the time domain, i.e., a curve that cuts the (θ_R,t) plane and which approximately separates the direct and delayed mechanisms. We denote such a curve by CC_T; an example is shown in red in Figure 2 for the H + D_2 reaction, again anticipating our results in section 4. CC_T has been superimposed on a contour plot of $\sigma(\theta_R,t)$ for $0 \le \theta_R/\text{deg} \le 180$ and $0 \le t/\text{fs} \le 123$. Note that the time-direct scattering will lie mainly to the left of CC_T in Figure 2 (i.e., at shorter times) while the time-delayed scattering is found mainly to the right (i.e., at longer times); this is clearly visible in the PWP movie of the time evolution of the reaction reported in refs 23 and 24. Other reactions also exhibit direct and delayed scattering, for example, F + HD → FH + D[25,26] and He + H_2^+ → HeH^+ + H.[32]

We decompose $f(\theta_R,t)$ into direct and delayed subamplitudes

$$f(\theta_R, t) = \bar{f}^{dir}(\theta_R, t) + \bar{f}^{del}(\theta_R, t) \tag{28}$$

where the overbars are to distinguish the $\bar{f}^{dir,del}(\theta_R,t)$ defined using CC_T from the subamplitudes, $f^{dir,del}(\theta_R,t)$, introduced in section 2C using CC_E filtering; see eq 21. The $\bar{f}^{dir,del}(\theta_R,t)$ are defined by applying overlapping filter functions, $\xi^{dir,del}(\theta_R,t)$, along CC_T together with a partition of unity. We have

$$\bar{f}^{del}(\theta_R, t) = \xi^{del}(\theta_R, t) f(\theta_R, t) = [1 - \xi^{dir}(\theta_R, t)] f(\theta_R, t) \tag{29}$$

and

$$\bar{f}^{\mathrm{dir}}(\theta_R, t) = \xi^{\mathrm{dir}}(\theta_R, t) f(\theta_R, t) \tag{30}$$

Note that $\xi^{\mathrm{dir}}(\theta_R,t) \rightarrow 1$ as $t \rightarrow 0$ and $\xi^{\mathrm{dir}}(\theta_R,t) \rightarrow 0$ as $t \rightarrow \infty$ at a fixed value of θ_R.

In a similar way to section 2C, we can also decompose the N,F subamplitudes, $f_{N,F}(\theta_R,t)$, into direct and delayed sub-subamplitudes

$$f_{N,F}(\theta_R, t) = \bar{f}_{N,F}{}^{\mathrm{dir}}(\theta_R, t) + \bar{f}_{N,F}{}^{\mathrm{del}}(\theta_R, t) \tag{31}$$

where

$$\bar{f}_{N,F}{}^{\mathrm{del}}(\theta_R, t) = \xi^{\mathrm{del}}(\theta_R, t) f_{N,F}(\theta_R, t) = [1 - \xi^{\mathrm{dir}}(\theta_R, t)] f_{N,F}(\theta_R, t) \tag{32}$$

and

$$\bar{f}_{N,F}{}^{\mathrm{dir}}(\theta_R, t) = \xi^{\mathrm{dir}}(\theta_R, t) f_{N,F}(\theta_R, t) \tag{33}$$

Overbars are again added to the $\bar{f}_{N,F}{}^{\mathrm{dir,del}}(\theta_R,t)$ to distinguish them from the $f_{N,F}{}^{\mathrm{dir,del}}(\theta_R,t)$ sub-subamplitudes defined by eq 23, which use CC_E filtering.

We next apply the inverse half-Fourier transform (11) to $\bar{f}^{\mathrm{dir,del}}(\theta_R,t)$ and $\bar{f}_{N,F}{}^{\mathrm{dir}}(\theta_R,t)$. This operation will provide us with filtered $\bar{f}^{\mathrm{dir,del}}(\theta_R,E)$ and $\bar{f}_{N,F}{}^{\mathrm{dir,del}}(\theta_R,E)$, respectively, where we use an overbar to distinguish them from eqs 18−21 and eqs 22−25, respectively. In particular we have

$$\bar{f}^{\mathrm{dir,del}}(\theta_R, E) = \frac{1}{2\pi\hbar F(E)} \int_0^\infty \bar{f}^{\mathrm{dir,del}}(\theta_R, t) \exp(iEt/\hbar)\, dt \tag{34}$$

and

$$\bar{f}_{N,F}{}^{\mathrm{dir,del}}(\theta_R, E) = \frac{1}{2\pi\hbar F(E)} \int_0^\infty \bar{f}_{N,F}{}^{\mathrm{dir,del}}(\theta_R, t) \exp(iEt/\hbar)\, dt \tag{35}$$

Filtered energy-domain DCSs can now be defined by

$$\bar{\sigma}^{\mathrm{dir,del}}(\theta_R, E) = |\bar{f}^{\mathrm{dir,del}}(\theta_R, E)|^2 \tag{36}$$

and

$$\bar{\sigma}_{N,F}{}^{\mathrm{dir,del}}(\theta_R, E) = |\bar{f}_{N,F}{}^{\mathrm{dir,del}}(\theta_R, E)|^2 \tag{37}$$

We can also define direct and delayed N,F LAMs by

$$\overline{\mathrm{LAM}}_{N,F}{}^{\mathrm{dir,del}}(\theta_R, E) = \frac{\partial \arg \bar{f}_{N,F}{}^{\mathrm{dir,del}}(\theta_R, E)}{\partial \theta_R} \tag{38}$$

In sections 4E and 4F we will use eqs 37 and 38 to study the effect that the CC_T filtration of $f_N(\theta_R,t)$ has on the properties of $\overline{\mathrm{LAM}}_N(\theta_R,E)$, and discuss its behavior in terms of the interfering sub-subamplitudes $\bar{f}_N{}^{\mathrm{dir}}(\theta_R,E)$ and $\bar{f}_N{}^{\mathrm{del}}(\theta_R,E)$.

We will call the filtration described in this section as "CC_T filtering" for brevity.

Identities. It is also convenient to extend the theory just presented by defining

$$\bar{f}(\theta_R, E) = \bar{f}^{\mathrm{dir}}(\theta_R, E) + \bar{f}^{\mathrm{del}}(\theta_R, E) \tag{39}$$

and

$$\bar{f}_{N,F}(\theta_R, E) = \bar{f}_{N,F}{}^{\mathrm{dir}}(\theta_R, E) + \bar{f}_{N,F}{}^{\mathrm{del}}(\theta_R, E) \tag{40}$$

together with

$$\bar{\sigma}(\theta_R, E) = |\bar{f}(\theta_R, E)|^2 \tag{41}$$

$$\overline{\mathrm{LAM}}(\theta_R, E) = \frac{\partial \arg \bar{f}(\theta_R, E)}{\partial \theta_R} \tag{42}$$

and

$$\bar{\sigma}_{N,F}(\theta_R, E) = |\bar{f}_{N,F}(\theta_R, E)|^2 \tag{43}$$

$$\overline{\mathrm{LAM}}_{N,F}(\theta_R, E) = \frac{\partial \arg \bar{f}_{N,F}(\theta_R, E)}{\partial \theta_R} \tag{44}$$

Then because a Fourier transform and its inverse are linear operations, we have the identities

$$f(\theta_R, E) \equiv \bar{f}(\theta_R, E) \tag{45}$$

$$\sigma(\theta_R, E) \equiv \bar{\sigma}(\theta_R, E) \tag{46}$$

$$\mathrm{LAM}(\theta_R, E) \equiv \overline{\mathrm{LAM}}(\theta_R, E) \tag{47}$$

and

$$f_{N,F}(\theta_R, E) \equiv \bar{f}_{N,F}(\theta_R, E) \tag{48}$$

$$\sigma_{N,F}(\theta_R, E) \equiv \bar{\sigma}_{N,F}(\theta_R, E) \tag{49}$$

$$\mathrm{LAM}_{N,F}(\theta_R, E) \equiv \overline{\mathrm{LAM}}_{N,F}(\theta_R, E) \tag{50}$$

However, in practice, the right-hand sides may differ from the corresponding left-hand sides, because of inevitable numerical errors that arise when the Fourier transforms and their inverses are performed. In this situation, comparing the right- and left-hand sides of eqs 45−50 provides a valuable check on the accuracy of the numerical calculations.

3. Calculations

A. Reactive Scattering Matrix Calculations. We use as input to our NF and LAM analyses, a set of accurate quantum scattering matrix elements, $\{\tilde{S}_J(E)\}$ for $J = 0$ (1) 40 with $\{\tilde{S}_J(E) \equiv 0\}$ for $J > 40$, on the energy grid, $E = 1.52$ (0.01) 2.50 eV. These matrix elements are the results of new wave packet scattering calculations[19] performed for the indistinguishable

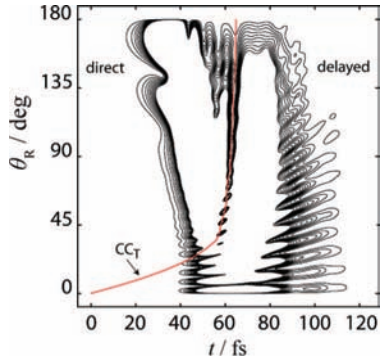

Figure 2. Contour plot of $\sigma(\theta_R,t)$. The values of the 10 contours are 9×10^{-12} (9×10^{-12}) 9×10^{-11} a_0^2 E_h^2 sr^{-1}. The red curve, called CC_T in the text, which is not a contour, approximately separates the direct and delayed scattering in the (θ_R,t) plane.

state-to-state $H + D_2$ reaction, using the potential energy surface number 2 of Boothroyd et al.[78] with masses of $m_H = 1.008$ u and $m_D = 2.014$ u. The total energy, E, is measured with respect to the classical minimum of the D_2 potential energy curve. This new set of $\{\tilde{S}_J(E)\}$ gives us better converged values for $f(\theta_R,E)$ at high E. (The previous calculations had $J = 0$ (1) 30 and used a smaller basis set.)

Note that the state-to-state reaction is closed for $E < E_{threshold} = 1.520$ eV, since the rovibrational energy, $E(v_i,j_i)$, of $D_2(v_i{=}0,j_i{=}0)$ is 0.192 eV and the rovibrational energy, $E(v_f,j_f)$, of $HD(v_f{=}3,j_f{=}0)$ is 1.520 eV.

B. Filter Functions. The PWP calculations used the same filter function, $F(E)$, as employed previously in ref 1. It is given by

$$F(E) = \frac{1}{2\sqrt{2\pi}} g(E) \exp\{i[k_i(E)z_i + k_f(E)z_f]\} \quad (51)$$

In eq 51, $k_i(E)$ and $k_f(E)$ are the initial and final translational wavenumbers, respectively, defined by $k_s(E) = \{2\,\mu_{X,YZ}[E - E(v_s,j_s)]\}^{1/2}/\hbar$ with $s = i, f$, where $\mu_{X,YZ} = m_X(m_Y + m_Z)/(m_X + m_Y + m_Z)$ is the reduced mass of the X + YZ channel. The distance z_i localizes the center of the initial PWP on the z axis with a width determined by $|F(E)|$. We used the value $z_i = -6$ a_0. Similarly we set $z_f = +6$ a_0, which distributes the centers of the probe PWPs around a sphere of radius 6 a_0 in the final channel. Finally, $g(E)$ is a distributed approximating function(al) (DAF)[79] defined by

$$g(E) \equiv g(M, E_0, \sigma, E) = \exp(-\bar{E}^2) \sum_{m=0}^{M/2} \frac{\bar{E}^{2m}}{m!} \quad (52)$$

where

$$\bar{E}^2 = \frac{1}{2}(E - E_0)^2\sigma^2 \quad (53)$$

with parameters of $M = 88$, $E_0 = 1.65$ eV, and $\sigma = 1/0.07$ eV^{-1} (n.b., σ is not related to the integral cross section). A plot of $g(E)$ is shown in Figure 3 for the set of parameters used in the filter function, $\xi^{del}(\theta_R,E)$, whose definition is considered next.

Equation 19 shows that the filter $\xi^{del}(\theta_R,E)$ is applied to $f(\theta_R,E)$ to produce $f^{del}(\theta_R,E)$. We denote the coordinates of CC_E in Figure 1 by $(\theta_R,E_{cut}(\theta_R))$. Then to filter the delayed mechanism out of $f(\theta_R,E)$, we use the DAF, $g(E)$, with parameters of $M = 2000$, $E_0 = 1.90$ eV and $\sigma = 100$ eV^{-1}. Figure 3 shows a plot of g(E) for these parameters. In addition, we require that the high E shoulder side of $g(E)$ takes the value 0.5 on the cut-curve, $E = E_{cut}(\theta_R)$, at each value of θ_R, i.e.

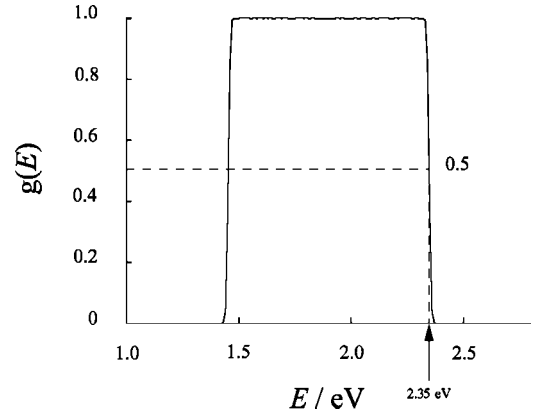

Figure 3. Plot of the distributed approximating function(al), $g(E)$ vs E. It is defined by eq 52 with parameters of $M = 2000$, $E_0 = 1.90$ eV, and $\sigma = 100$ eV^{-1}. The dashed line indicates that $g(E) = 0.5$ for $E = 2.35$ eV.

$$\xi^{del}(\theta_R, E = E_{cut}(\theta_R)) = g(E = E_{cut}(\theta_R)) = 0.5 \quad (54)$$

This is achieved by adjusting the value of $E_0 = E_0(\theta_R)$ in eq 53 (keeping σ fixed) until eq 54 is satisfied. For example, for the cut-curve drawn in red in Figure 1, we used $E_0(\theta_R) = E_{cut}(\theta_R) - 0.44736$ eV. It is also necessary to check that $\xi^{del}(\theta_R,E) = 1$ at low values of θ_R and E; if not, a correction is made.

The filter function, $\xi^{dir}(\theta_R,t)$, in the time domain, which is used to filter $f(\theta_R,t)$ in eq 30 is defined by analogy with eqs 52 and 53. Thus we first define the DAF

$$g(t) \equiv g(M, t_0, \rho, t) = \exp(-\bar{t}^2) \sum_{m=0}^{M/2} \frac{\bar{t}^{2m}}{m!} \quad (55)$$

where

$$\bar{t}^2 = \frac{1}{2}(t - t_0)^2\rho^2 \quad (56)$$

with parameters of $M = 88$ and $\rho = 0.2092$ fs^{-1}. We denote the coordinates of the cut-curve, CC_T, in the time domain by $(\theta_R,t_{cut}(\theta_R))$—see the red curve in Figure 2. By analogy with $\xi^{del}(\theta_R,E)$, we require that $\xi^{dir}(\theta_R,t)$ is equal to 0.5 on CC_T. This is achieved by adjusting the value of $t_0 = t_0(\theta_R)$ at each value of θ_R in eq 56 until we have for the high shoulder side of $\xi^{dir}(\theta_R,t)$

$$\xi^{dir}(\theta_R, t = t_{cut}(\theta_R)) = g(t = t_{cut}(\theta_R)) = 0.5 \quad (57)$$

The equations in section 2 were then evaluated using numerical techniques that have been described previously, e.g., refs 1 and 2.

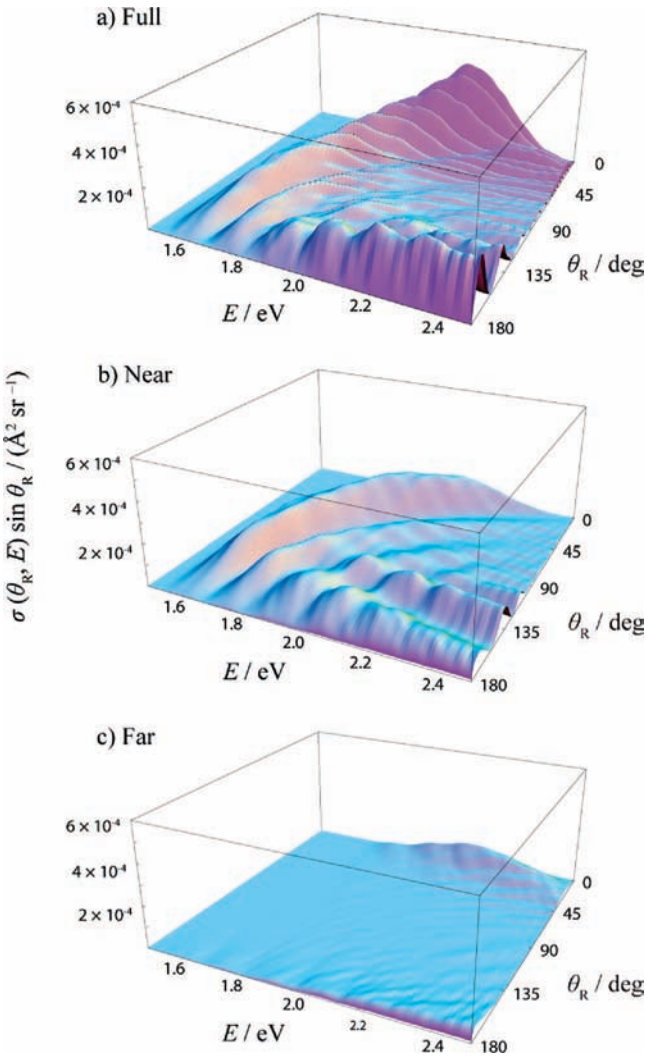

Figure 4. Perspective plots of (a) $\sigma(\theta_R,E)$ sin θ_R, (b) $\sigma_N(\theta_R,E)$ sin θ_R, and (c) $\sigma_F(\theta_R,E)$ sin θ_R vs θ_R and E.

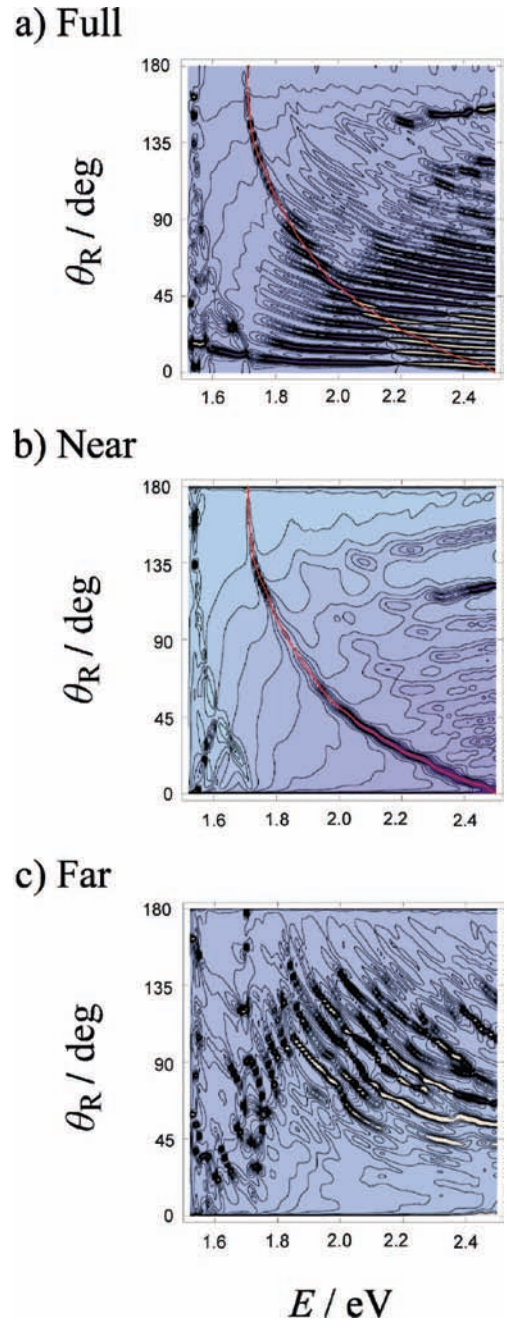

Figure 5. LAM contour plots for (a) LAM(θ_R,E). The red curve indicates the location of the center of the trench in panel b, (b) $LAM_N(\theta_R,E)$. The red curve indicates the location of the center of the trench, and (c) $LAM_F(\theta_R,E)$. The values of the 27 contours in each panel are −39 (3) 39.

4. Results

This section presents our results using the theory developed in section 2. Most of the results will be displayed graphically. It is helpful to remember that direct and delayed DCSs with an overbar, i.e., $\bar{\sigma}^{dir,del}(\theta_R,E)$, have used CC_T filtering in their construction, whereas angular distributions without an overbar, i.e., $\sigma^{dir,del}(\theta_R,t)$, have employed CC_E filtering.

A. Full and Nearside−Farside Differential Cross Sections in the Energy Domain. Parts a−c of Figure 4 show perspective plots of $\sigma(\theta_R,E)$ sin θ_R, $\sigma_N(\theta_R,E)$ sin θ_R and $\sigma_F(\theta_R,E)$ sin θ_R, respectively, using eqs 1−6. The DCSs have been multiplied by sin θ_R in order to contain large features in the scattering close to $\theta_R = 0°$ and $\theta_R = 180°$. Note that the relation between $\sigma_N(\theta_R,E)$, $\sigma_F(\theta_R,E)$, and $\sigma(\theta_R,E)$ is readily obtained from eqs 2, 3, and 6 and is called the *fundamental NF identity for cross sections*.[57] It is given by

$$\sigma(\theta_R,E) = \sigma_N(\theta_R,E) + \sigma_F(\theta_R,E) + 2[\sigma_N(\theta_R,E) \times \sigma_F(\theta_R,E)]^{1/2} \cos[\arg f_N(\theta_R,E) - \arg f_F(\theta_R,E)] \quad (58)$$

The results in Figure 4 are similar to those reported earlier in Figure 1 of ref 2 and the same comments apply. Briefly, the backward scattering is N dominated, whereas the pronounced oscillations as a function of θ_R in the forward scattering are caused by interference of the more slowly varying N and F subamplitudes. The forward scattering at $E = 2.00$ eV has been analyzed in detail using semiclassical techniques in refs 51, 53, 54, 56, and 64 where the oscillations have been proven to be part of a forward glory. At large angles, Figure 4 shows there are slow undulations in $\sigma(\theta_R,E)$ sin θ_R as a function of E. Similar undulations occur in $\sigma_N(\theta_R,E)$ sin θ_R, and so they do not arise from NF interference. It has been suggested that the origin of these undulations is interference between contributions to the overall reaction from quantized transition states.[80] The scattering at 180° for $\sigma(\theta_R,E)$ cannot be seen in Figure 4; we will examine it in more detail in section 4D.

Next we consider how to define a cut-curve for $\sigma(\theta_R,E)$ or $\sigma_{N,F}(\theta_R,E)$ in order to filter (bisect) $f(\theta_R,E)$ into a "direct" part, which is the energy-domain analogue of the time-direct scattering, plus a "delayed" part, which is the energy-domain analogue of the time-delayed scattering. On general grounds, we expect scattering into backward angles to correspond to a direct mechanism, with scattering into forward angles corresponding to a delayed mechanism. Unfortunately when we examine Figure 4, there is no obvious feature in $\sigma(\theta_R,E)$ or $\sigma_{N,F}(\theta_R,E)$ that lets us define a dynamically meaningful cut-curve with the desired property. However, we will see in the next section that the situation is different when we examine plots of $LAM(\theta_R,E)$ and $LAM_{N,F}(\theta_R,E)$.

B. Full and Nearside−Farside Local Angular Momenta in the Energy Domain. Parts a−c of Figure 5 show contour plots of $LAM(\theta_R,E)$, $LAM_N(\theta_R,E)$, and $LAM_F(\theta_R,E)$ respectively, using eqs 7 and 8. In contrast to the corresponding contour plot of $\sigma_N(\theta_R,E)$ in Figure 4b, we now see a distinctive, well-defined, feature in $LAM_N(\theta_R,E)$, namely, a pronounced negative trench starting at ($\theta_R \approx 180°$,$E = 1.71$ eV) and moving through the (θ_R,E) plane to ($\theta_R \approx 0°$,$E = 2.50$ eV). This trench, which bisects the (θ_R,E) plane, is seen very clearly in the perspective view of $LAM_N(\theta_R,E)$ in Figure 6.

We now use the center of the trench to define, by eye, a cut-curve, CC_E, to approximately separate the two reaction mechanisms, which are the energy-domain analogues of the time-direct and time-delayed scattering. CC_E is drawn as a red curve in Figure 5b, where it is superimposed on the contour plot of $LAM_N(\theta_R,E)$. The full $LAM(\theta_R,E)$, which is N dominated, is seen to exhibit a similar dynamical feature in Figure 5a; CC_E is again superimposed on its contour plot as a red curve. The cut-curve drawn in parts a and b of Figure 5 is the same as the one we used in our discussion of Figure 1 (where it was also drawn as a red curve). We examine the dynamical consequences of using CC_E to filter the reaction mechanisms in the next section.

Our results in Figure 5 for the trench and CC_E are generally similar to those we reported earlier in Figure 10 of ref 2, with an important exception. Previously the trench in the contour plot of $LAM_N(\theta_R,E)$ became a ridge for a narrow range of energies, $E \approx 2.05-2.20$ eV, giving rise to a "trench-ridge" effect rather than a "trench" effect. Evidently, the DCS and LAM calculations in refs 1 and 2 and those in the present paper provide an example where the full and N,F local angular momenta are more sensitive to small changes in the numerical values of the scattering matrix elements than are the full and N,F cross sections; this sensitivity of LAMs has been pointed out before.[49]

Finally, it should be noted that the relation between $LAM_N(\theta_R,E)$, $LAM_F(\theta_R,E)$, and $LAM(\theta_R,E)$ is given by the *fundamental NF identity for local angular momenta*, which can be written in the form[57]

$$\begin{aligned} LAM(\theta_R,E)\sigma(\theta_R,E) = LAM_N(\theta_R,E)\sigma_N(\theta_R,E) + \\ LAM_F(\theta_R,E)\sigma_F(\theta_R,E) + C(\theta_R,E) \end{aligned} \quad (59)$$

where the NF term $C(\theta_R,E)$ is defined explicitly in ref 57. The properties of this identity have been examined in detail[57] at $E = 2.00$ eV, making use of the concept of a CLAM (cross section × LAM) plot.

C. Direct and Delayed Angular Distributions in the Time Domain Obtained by CC_E Filtering. Having defined CC_E in section 4B, we now follow the theory of section 2C to filter the direct and delayed scattering amplitudes in the energy domain, which we then map to the time domain by a half-Fourier transform; see eqs 9, 10, 18−21, and 26. Figure 7 shows perspective plots of $\sigma(\theta_R,t)$ sin θ_R, $\sigma^{dir}(\theta_R,t)$ sin θ_R, and $\sigma^{del}(\theta_R,t)$ sin θ_R for $t = 0$ fs to $t = 123$ fs. The angular distributions have been multiplied by sin θ_R in order to contain large features in the scattering close to $\theta_R = 0°$ and $\theta_R = 180°$.

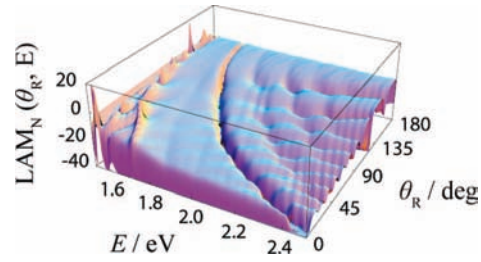

Figure 6. Perspective plot of $LAM_N(\theta_R,E)$ vs θ_R and E.

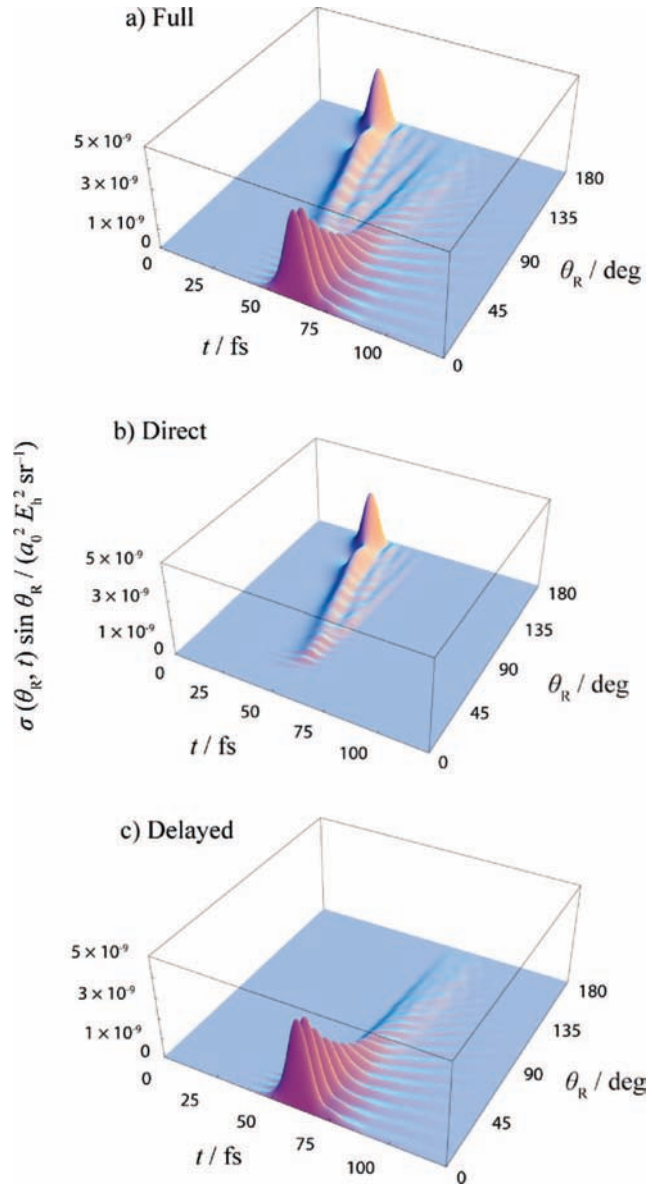

Figure 7. Perspective plots of (a) $\sigma(\theta_R,t)$ sin θ_R, (b) $\sigma^{dir}(\theta_R,t)$ sin θ_R, and (c) $\sigma^{del}(\theta_R,t)$ sin θ_R vs θ_R and t.

Figure 7a shows that two mechanisms contribute to the reaction:[1,23,24] direct scattering which results in a large peak in the backward angular region, and delayed scattering which causes a large oscillatory peak in the forward region after a delay of about 25 fs. NF analysis of the time-dependent angular

distributions in ref 1 showed that the forward angle oscillations arise from NF interference. It is likely that these oscillations can be interpreted as a glory, although it would be necessary to carry out a uniform semiclassical analysis to prove this interpretation. We can see that the two mechanisms are not disjoint; rather there is interference between them. Note also that Figure 2 is a contour plot of Figure 7a.

Parts b and c of Figure 7 show that CC_E filtering has approximately separated the two time-distinct mechanisms. This is an important finding because it demonstrates that the location of the center of the trench in $LAM_N(\theta_R,E)$ (used to filter $f(\theta_R,E)$) has successfully identified the analogues of the direct and delayed mechanisms in the energy domain without first examining the properties of $\sigma(\theta_R,t)$. It also justifies our use of the labels "direct" and "delayed" from section 2C onward.

D. Direct and Delayed Differential Cross Sections in the Energy Domain Obtained by CC_T Filtering. We now consider the reverse process: How to define a cut-curve CC_T in the (θ_R,t) plane in order to approximately separate $f(\theta_R,t)$ into two mechanisms? Then we map $\bar{f}^{dir}(\theta_R,t)$ and $\bar{f}^{del}(\theta_R,t)$ to the energy domain by the inverse Fourier transform (34) to give $\bar{f}^{dir}(\theta_R,E)$ and $\bar{f}^{del}(\theta_R,E)$, respectively. Our results in sections 4B and 4C using the CC_E filter allow us to remove some of the ambiguity in the specification of CC_T. (cf. ref 24 in which a cut-curve is found by trial and error methods applied to the full angular distribution, $\sigma(\theta_R,t)$).

The CC_T we use is one we displayed earlier in our discussion of Figure 2, where it is drawn as a red curve. At large angles, it can be seen that CC_T follows the deepest (interference) trench between the direct and delayed scattering; it then moves through the (θ_R,t) plane to ($\theta_R = 0°$, $t = 0$ fs). The cut-curve used in Figure 3 of ref 24 or Figure 1 of ref 31 is similar to CC_T except that it lies closer to the direct angular distribution at large angles and to the delayed angular distribution at small angles.

Parts a−c of Figure 8 show perspective plots of $\bar{\sigma}(\theta_R,E)$ sin θ_R, $\bar{\sigma}^{dir}(\theta_R,E)$ sin θ_R, and $\bar{\sigma}^{del}(\theta_R,E)$ sin θ_R, respectively, using eqs 39, 41, and 43. Note that the energy scale in Figure 8 goes to E/eV = 2.30 rather than E/eV = 2.50 as in Figures 1 and 4−6. This is because the inverse Fourier transform (34) becomes numerically unstable when $|F(E)|$ is small. For example, at E = 2.50 eV, we have $|F(E)| = 2.6 \times 10^{-5}$.

We note first that Figure 8a for $\bar{\sigma}(\theta_R,E)$ sin θ_R is essentially the same as Figure 4a, which displays $\sigma(\theta_R,E)$ sin θ_R; this agreement provides a valuable check on the accuracy of our numerical procedures for the half-Fourier transform and its inverse. Second, parts b and c of Figure 8 show that the CC_T filtering has produced direct and delayed DCSs in the energy domain which are consistent with Figure 1 when $\sigma(\theta_R,E)$ is cut along CC_E.

The scattering at $\theta_R = 180°$ is not visible in Figure 8. It is displayed in Figure 9 which plots $\bar{\sigma}(180°,E)$, $\bar{\sigma}^{dir}(180°,E)$, and $\bar{\sigma}^{del}(180°,E)$ for 1.52 eV ≤ E ≤ 2.40 eV, as well as $\sigma(180°,E)$ for 1.52 eV ≤ E ≤ 2.50 eV. We see that $\bar{\sigma}(180°,E)$ and $\sigma(180°,E)$ agree closely, which provides another important check on our numerics. $\bar{\sigma}(180°,E)$ possesses nine peaks and nine dips, and it is evident that this structure arises from interference between the direct and delayed mechanisms (i.e., $\bar{f}^{dir}(180°,E)$ and $\bar{f}^{del}(180°,E)$), with the direct scattering being the dominant contributor. Note that $\bar{\sigma}^{dir}(180°,E)$ possesses weak undulations at higher values of E. The results in Figure 9 are consistent with the conclusions of ref 24 which uses a different CC_T.

E. Nearside Scattering in the Energy Domain: Direct and Delayed Differential Cross Sections and Local Angular

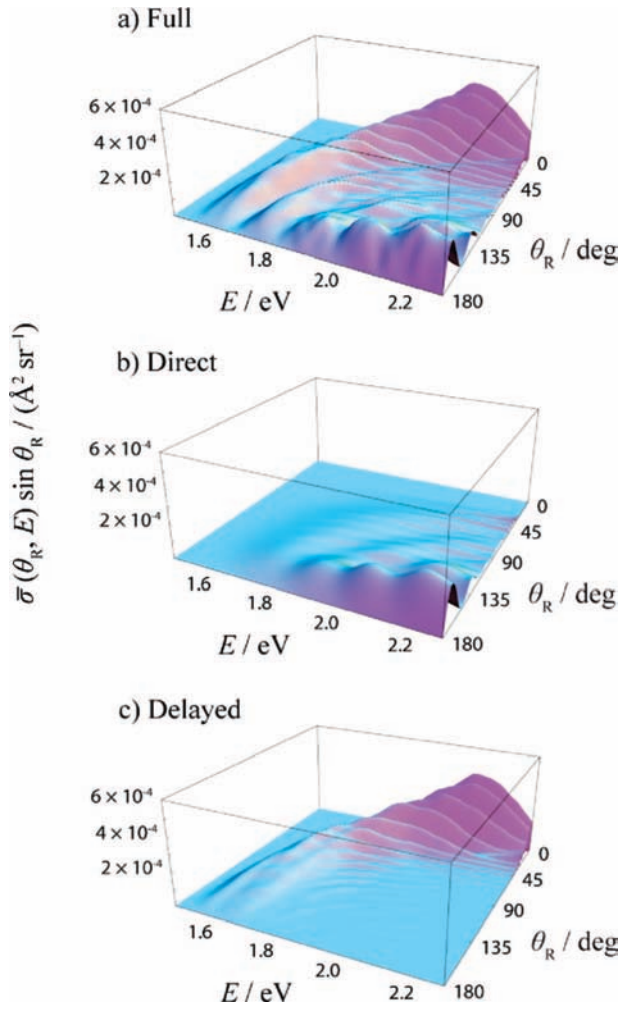

Figure 8. Perspective plots of (a) $\bar{\sigma}(\theta_R,E)$ sin θ_R, (b) $\bar{\sigma}^{dir}(\theta_R,E)$ sin θ_R, and (c) $\bar{\sigma}^{del}(\theta_R,E)$ sin θ_R vs θ_R and E.

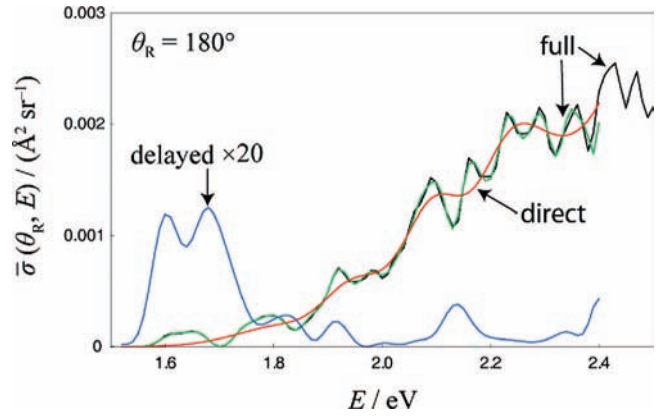

Figure 9. Plots of $\bar{\sigma}(\theta_R,E)$(green), $\bar{\sigma}^{dir}(\theta_R,E)$(red), and $\bar{\sigma}^{del}(\theta_R,E)$ (blue) vs E at $\theta_R = 180°$ for 1.52 ≤ E /eV ≤ 2.40. Also plotted is $\sigma(\theta_R = 180°,E)$ (black) for 1.52 ≤ E /eV ≤ 2.50.

Momenta Obtained by CC_T Filtering. It was emphasized in section 4B that the nearside scattering in the energy domain is very important for identifying the direct and delayed mechanisms, and in this section we examine their contribution to the N DCS. Figure 10 shows perspective plots of $\bar{\sigma}_N(\theta_R,E)$ sin θ_R, $\bar{\sigma}_N^{dir}(\theta_R,E)$ sin θ_R and $\bar{\sigma}_N^{del}(\theta_R,E)$ sin θ_R. These plots were obtained (1) by decomposing $f(\theta_R,t)$ into $f_N(\theta_R,t) + f_F(\theta_R,t)$ using eq 16, (2) by filtering $f_N(\theta_R,t)$ with CC_T to produce $\bar{f}_N^{dir}(\theta_R,t) + \bar{f}_N^{del}(\theta_R,t)$—see eqs 31−33, (3) by applying the inverse half-Fourier transform (35) to generate $\bar{f}_N^{dir}(\theta_R,E)$ and $\bar{f}_N^{del}(\theta_R,E)$, and

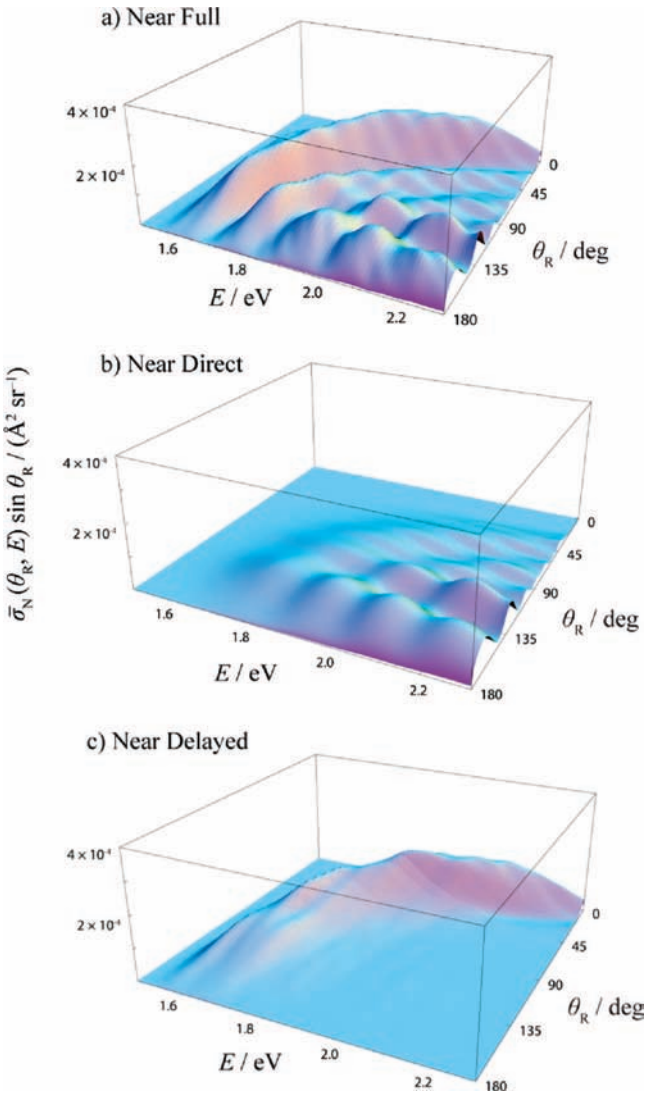

Figure 10. Perspective plots of (a) $\bar{\sigma}_N(\theta_R,E)$ sin θ_R, (b) $\bar{\sigma}_N{}^{dir}(\theta_R,E)$ sin θ_R, and (c) $\bar{\sigma}_N{}^{del}(\theta_R,E)$ sin θ_R vs θ_R and E.

finally (4) the direct, delayed, and full N DCSs are calculated from eqs 37, 40, and 43.

Figure 10a for $\bar{\sigma}_N$ (θ_R,E) sin θ_R is very similar to $\sigma_N(\theta_R,E)$ sin θ_R in Figure 4b which verifies the accuracy of our numerical methods. Parts b and c of Figure 10 show that CC_T filtering has produced direct and delayed N DCSs in the energy domain which are consistent with $\sigma_N(\theta_R,E)$ (or $\bar{\sigma}_N(\theta_R,E)$) being cut along CC_E. Note that $\bar{\sigma}^{del}(\theta_R,E)$ in Figure 8c has rapid oscillations in the forward angle region, whereas $\bar{\sigma}_N{}^{del}(\theta_R,E)$ in Figure 10c does not. This demonstrates that F scattering, by interfering with the N scattering, is responsible for the forward-angle glory oscillations.

Figure 11 presents a more detailed examination at $E = 2.00$ eV of the angular dependence of the direct and delayed N DCSs, as well as the full N DCS. This plot shows there is a minimum in $\bar{\sigma}_N(\theta_R,$ 2.00 eV) at $\theta_R \approx 50°$, which is very close to the location of CC_E at this energy; see Figure 1. The trough in $\bar{\sigma}_N(\theta_R,$ 2.00 eV) evidently arises from the interference of $\bar{f}_N{}^{dir}(\theta_R,$ 2.00 eV) with $\bar{f}_N{}^{del}(\theta_R,$ 2.00 eV), since $\bar{\sigma}_N{}^{dir}(\theta_R,$ 2.00 eV) and $\bar{\sigma}_N{}^{del}(\theta_R,$ 2.00 eV) are slowly varying functions of θ_R around $\theta_R = 50°$. We also see that $\bar{\sigma}_N{}^{dir}(\theta_R,$2.00 eV) dominates the scattering at sideward and backward angles, with a steep fall off in the forward intensity for $\theta_R \lesssim 30°$. In contrast, $\bar{\sigma}_N{}^{del}(\theta_R,$ 2.00 eV) shows enhanced forward scattering with relatively little sideward and backward scattering.

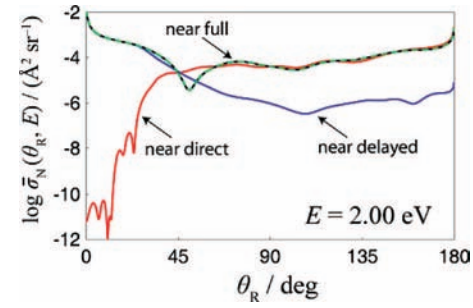

Figure 11. Plots of log $\bar{\sigma}_N(\theta_R,E)$ (dashed green), log $\bar{\sigma}_N{}^{dir}(\theta_R,E)$ (red), and log $\bar{\sigma}_N{}^{del}(\theta_R,E)$ (blue) vs θ_R at $E = 2.00$ eV. Also plotted is log $\sigma_N(\theta_R,E = 2.00$ eV) (black) vs θ_R; it overlaps with the curve for log $\bar{\sigma}_N(\theta_R,E = 2.00$ eV) on the scale of the drawing.

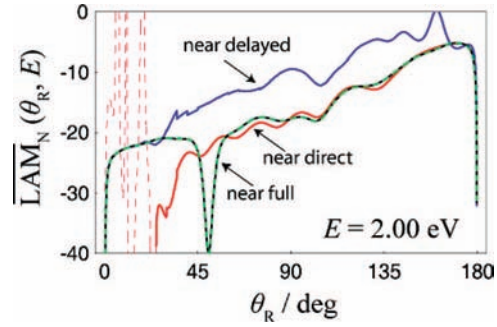

Figure 12. Plots of $\overline{LAM}_N(\theta_R,E)$ (dashed green), $\overline{LAM}_N{}^{dir}(\theta_R,E)$ (red), and $\overline{LAM}_N{}^{del}(\theta_R,E)$ (blue) vs θ_R at $E = 2.00$ eV. The dashed red curve indicates where $\overline{LAM}_N{}^{dir}(\theta_R,E = 2.00$ eV) becomes unphysical. Also plotted is $LAM_N(\theta_R,E = 2.00$ eV) (black) vs θ_R; it overlaps with the curve for $\overline{LAM}_N(\theta_R,E = 2.00$ eV) on the scale of the drawing.

Figure 12 displays graphs of $\overline{LAM}_N{}^{dir}(\theta_R,E)$, $\overline{LAM}_N{}^{del}(\theta_R,E)$, and $\overline{LAM}_N(\theta_R,E)$ versus θ_R at $E = 2.00$ eV using eqs 38 and 44. We see that the trench in $\overline{LAM}_N(\theta_R,$2.00 eV) at $\theta_R \approx 50°$ has been smoothed in both $\overline{LAM}_N{}^{dir}(\theta_R,$2.00 eV) and $\overline{LAM}_N{}^{del}(\theta_R,$ 2.00 eV). At larger angles beyond the trench we have $\overline{LAM}_N(\theta_R,$ 2.00 eV) $\approx \overline{LAM}_N{}^{dir}(\theta_R,$2.00 eV) and at smaller angles $\overline{LAM}_N(\theta_R,$ 2.00 eV) $\approx \overline{LAM}_N{}^{del}(\theta_R,$ 2.00 eV). These properties are consistent with the behavior of the N DCSs in Figure 11. Beyond the trench angular region in Figure 12, the overall trend for the moduli of the three N LAMs is toward smaller values as θ_R increases; this is the expected behavior for N scattering.[52] The dashed line in Figure 12, at small values of θ_R, indicates where $\overline{LAM}_N{}^{dir}(\theta_R,$2.00 eV) exhibits erratic oscillatory behavior and is unphysical. Now Figure 11 shows that $\bar{\sigma}_N{}^{dir}(\theta_R,$ 2.00 eV) is very small in this angular region (where the time-delayed mechanism is dominant), which means that $\bar{f}_N{}^{dir}(\theta_R,$ 2.00 eV) is likely to contain increased numerical noise as a result of the CC_T filtering. This numerical noise is passed on to $\overline{LAM}_N{}^{dir}(\theta_R,$2.00 eV) through the derivative of the phase of $\bar{f}_N{}^{dir}(\theta_R,$2.00 eV)- see eq 38.

F. Nearside Scattering in the Energy Domain: Direct and Delayed Interference Effects in the Trench Feature Belonging to the Local Angular Momentum. We finally study Argand plots of the scattering subamplitude, $\bar{f}_N(\theta_R,E)$, and the sub-subamplitudes, $\bar{f}_N{}^{dir}(\theta_R,E)$ and $\bar{f}_N{}^{del}(\theta_R,E)$ at $E = 2.00$ eV in order to better understand the observation that $LAM(\theta_R,E)$, and particularly $LAM_N(\theta_R,E)$, exhibit a trench around CC_E in Figures 5 and 6. Note from eq 40 that

$$\bar{f}_N(\theta_R, E) = \bar{f}_N{}^{dir}(\theta_R, E) + \bar{f}_N{}^{del}(\theta_R, E)$$

We also recall from eqs 48 and 50 that $f_N(\theta_R,E) \equiv \bar{f}_N(\theta_R,E)$ and $LAM_N(\theta_R,E) \equiv \overline{LAM}_N(\theta_R,E)$, respectively, apart from inevitable

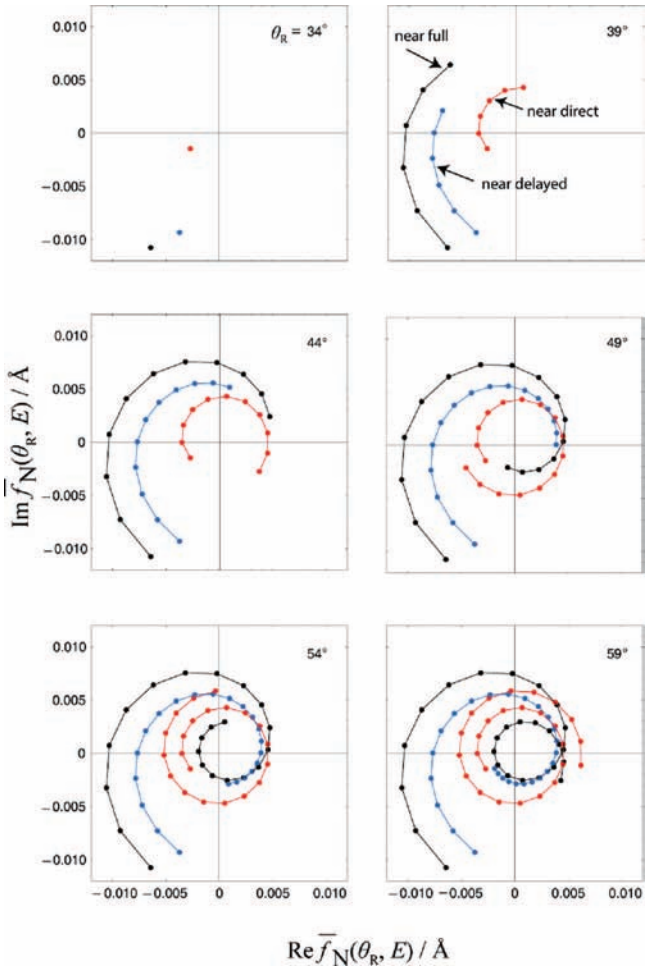

Figure 13. Snapshots from a movie of Argand plots of $\bar{f}_N(\theta_R,E)$ (black), $\bar{f}_N^{dir}(\theta_R,E)$ (red), and $\bar{f}_N^{del}(\theta_R,E)$ (blue) at $E = 2.00$ eV. Each solid circle represents an incremental step in θ_R of 1°. Each snapshot shows all increments from $\theta_R = 34°$ up to $\theta_R = 34°$, 39°, 44°, 49°, 54°, and 59°.

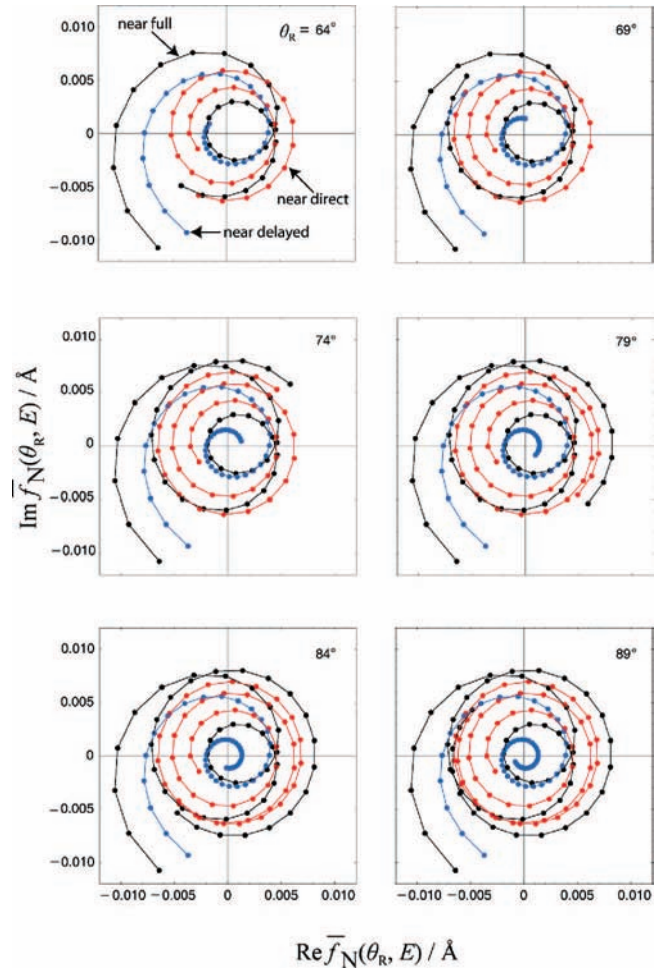

Figure 14. Snapshots from a movie of Argand plots of $\bar{f}_N(\theta_R,E)$ (black), $\bar{f}_N^{dir}(\theta_R,E)$ (red), and $\bar{f}_N^{del}(\theta_R,E)$ (blue) at $E = 2.00$ eV. Each solid circle represents an incremental step in θ_R of 1°. Each snapshot shows all increments from $\theta_R = 34°$ up to $\theta_R = 64°$, 69°, 74°, 79°, 84°, and 89°.

numerical errors associated with the half-Fourier transform and its inverse. In our computations, we always found that $f_N(\theta_R,E)$ and $\bar{f}_N(\theta_R,E)$ agreed to within graphical accuracy.

With Mathematica 5.1, an animated movie of Argand plots for the three subamplitudes has been made at $E = 2.00$ eV, whereby each successive frame corresponds to an increase in θ_R of 1°. Figures 13 and 14 show snapshots from the movie for $\theta_R = 34°$ (5°) 89°. Examination of the movie and Figures 13 and 14 leads to the following observations (where $E = 2.00$ eV in all cases):

$\bar{f}_N^{del}(\theta_R,E)$ (blue) spirals inward as θ_R increases while $\bar{f}_N^{dir}(\theta_R,E)$ (red) spirals out. $\bar{f}_N(\theta_R,E)$ (black) initially spirals in until $\theta_R \approx 50°$, when it begins to spiral out.

$\bar{f}_N(\theta_R,E)$ behaves at first like $\bar{f}_N^{del}(\theta_R,E)$, i.e., the moduli, phases, and LAMs are similar. We see that $|\bar{f}_N^{dir}(\theta_R,E)|$ is small.

As θ_R increases, $\bar{f}_N(\theta_R,E)$ begins to exhibit more of the characteristics of $\bar{f}_N^{dir}(\theta_R,E)$. By $\theta_R \approx 49°$, the phase of $\bar{f}_N(\theta_R,E)$ has started to "catch up" with the phase of $\bar{f}_N^{dir}(\theta_R,E)$. This results in a more negative value of $\overline{LAM}_N(\theta_R,E)$, since the phase of $\bar{f}_N(\theta_R,E)$ decreases faster than previously observed.

By $\theta_R \approx 52°$, the phase of $\bar{f}_N(\theta_R,E)$ has caught up with the phase of $\bar{f}_N^{dir}(\theta_R,E)$. We see that $|\bar{f}_N^{dir}(\theta_R,E)|$ and $|\bar{f}_N^{del}(\theta_R,E)|$ are of similar magnitudes.

Next, the phase of $\bar{f}_N(\theta_R,E)$ overtakes the phase of $\bar{f}_N^{dir}(\theta_R,E)$ and then slows down, with the result that $\overline{LAM}_N(\theta_R,E)$ becomes less negative. By $\theta_R \approx 89°$, $f_N(\theta_R,E)$ behaves like $\bar{f}_N^{dir}(\theta_R,E)$; i.e., the moduli, phases, and LAMs are similar. We see that $|\bar{f}_N^{del}(\theta_R,E)|$ is small.

From these observations, we see that the trench structure at $E = 2.00$ eV is caused by a transfer in behavior of $\bar{f}_N(\theta_R,E)$ from delayed dynamics to direct dynamics as θ_R increases. This is a destructive interference effect which requires the phase of $\bar{f}_N(\theta_R,E)$ to decrease faster with respect to θ_R to overtake the phase of $\bar{f}_N^{dir}(\theta_R,E)$, resulting in a minimum in $\overline{LAM}_N(\theta_R,E)$ around $\theta_R = 50°$.

5. Conclusions

We have presented the results of NF angular distributions and NF LAM analyses for the H + $D_2(v_i = 0, j_i = 0, m_i = 0)$ → HD($v_f = 3, j_f = 0, m_f = 0$) + D reaction in the energy and time domains. Our calculations used a new set of accurate quantum scattering matrix elements.

We discovered that $LAM(\theta_R,E)$, and in particular $LAM_N(\theta_R,E)$, exhibit a pronounced dynamical feature, namely, a negative trench that bisects the (θ_R,E) plane. We used the location of this trench to design a filter to approximately separate two reaction mechanisms. Transforming to the time domain showed that these two reaction mechanisms are the energy-domain analogues of direct and delayed scattering, which interfere to produce the trench. This is the first successful

filtration of reaction mechanisms carried out directly in the (θ_R,E) domain. Our approach also allows us to remove some (though not all) of the ambiguity in previous definitions of CC_T. We have demonstrated that combining the PWP theory of time dependent scattering with NF and LAM analyses provides a powerful tool for filtering mechanisms in quantum reactive scattering.

Acknowledgment. We thank Dr. S. C. Althorpe (University of Cambridge) for his help and advice on the PWP theory of time-dependent scattering. We also thank Dr. A. J. Totenhofer (University of Manchester) for his help with the figures. Support of this research by the U.K. Engineering and Physical Sciences Research Council is gratefully acknowledged.

References and Notes

(1) Monks, P. D. D.; Connor, J. N. L.; Althorpe, S. C. *J. Phys. Chem. A* **2006**, *110*, 741.
(2) Monks, P. D. D.; Connor, J. N. L.; Althorpe, S. C. *J. Phys. Chem. A* **2007**, *111*, 10302.
(3) Clary, D. C. *Proc. Nat. Acad. Sci.* **2008**, *105*, 12649.
(4) Yang, X. *Annu. Rev. Phys. Chem.* **2007**, *58*, 433.
(5) Dai, D.; Yang, X. *Huaxue Jinzhan* **2007**, *19*, 1633.
(6) Hu, W.; Schatz, G. C. *J. Chem. Phys.* **2006**, *125*, 132301.
(7) Semiclassical and Other Methods for Understanding Molecular Collisions and Chemical Reactions. *Collaborative Computational Project on Molecular Quantum Dynamics*; Sen, S., Sokolovski, D., Connor, J. N. L., Eds.; Collaborative Computational Project Number 6; CCP6, Daresbury Laboratory, Warrington, U.K., 2005. ISBN 0-9545289-3-X.
(8) Theory of Chemical Reaction Dynamics. *Proceedings of the NATO Advanced Research Workshop on Theory of the Dynamics of Elementary Chemical Reactions, Balatonföldár, Hungary, 8−12 June, 2003*; Laganà, A., Lendvay, G., Eds.; Kluwer: Dordrecht, The Netherlands, 2004.
(9) *Modern Trends in Chemical Reaction Dynamics, Experiment and Theory*; Parts I and II; Yang. X., Liu, K., Eds.; World Scientific: Singapore, 2004.
(10) Althorpe, S. C.; Clary, D. C. *Annu. Rev. Phys. Chem.* **2003**, *54*, 493.
(11) Nyman, G.; Yu, H.-G. *Rep. Prog. Phys.* **2000**, *63*, 1001.
(12) Aoiz, F. J.; Bañares, L.; Herrero, V. J. *Int. Rev. Phys. Chem.* **2005**, *24*, 119.
(13) Bañares, L.; Aoiz, F. J.; Herrero, V. J. *Phys. Scr.* **2006**, *73*, C6.
(14) Goldberg, N. T.; Zhang, J.; Miller, D. J.; Zare, R. N. *J. Phys. Chem. A* **2008**, *112*, 9266.
(15) Greaves, S. J.; Murdock, D.; Wrede, E. *J. Chem. Phys.* **2008**, *128*, 164307.
(16) Greaves, S. J.; Murdock, D.; Wrede, E.; Althorpe, S. C. *J. Chem. Phys.* **2008**, *128*, 164306.
(17) Chu, T.-S.; Han, K.-L. *Phys. Chem. Chem. Phys.* **2008**, *10*, 2431.
(18) Chu, T.-S.; Han, K.-L.; Hankel, M.; Balint-Kurti, G. G. *J. Chem. Phys.* **2008**, *126*, 214303.
(19) Koszinowski, K.; Goldberg, N. T.; Zhang, J.; Zare, R. N.; Bouakline, F.; Althorpe, S. C. *J. Chem. Phys.* **2007**, *127*, 124315.
(20) Goldberg, N. T.; Koszinowski, K.; G.; Pomerantz, A. E.; Zare, R. N. *Chem. Phys. Lett.* **2007**, *433*, 439.
(21) Lu, R. F.; Chu, T.-S.; Zhang, Y.; Han, K.-L.; Varandas, A. J. C.; Zhang, J. Z. H. *J. Chem. Phys.* **2006**, *125*, 133108.
(22) Aldegunde, J.; Alvariño, J. M.; Kendrick, B. K.; Sáez Rábanos, V.; de Miranda, M. P.; Aoiz, F. J. *Phys. Chem. Chem. Phys.* **2006**, *8*, 4881.
(23) Althorpe, S. C.; Fernández-Alonso, F.; Bean, B. D.; Ayers, J. D.; Pomerantz, A. E.; Zare, R. N.; Wrede, E. *Nature (London)* **2002**, *416*, 67.
(24) Althorpe, S. C. *J. Chem. Phys.* **2002**, *117*, 4623.
(25) Althorpe, S. C. *Chem. Phys. Lett.* **2003**, *370*, 443.
(26) Althorpe, S. C. *J. Phys. Chem. A* **2003**, *107*, 7152.
(27) Juanes-Marcos, J. C.; Althorpe, S. C. *Chem. Phys. Lett.* **2003**, *381*, 743.
(28) Althorpe, S. C. *Phys. Rev. A* **2004**, *69*, 042702.
(29) Althorpe, S. C. *J. Chem. Phys.* **2004**, *121*, 1175.
(30) Althorpe, S. C. *Int. Rev. Phys. Chem.* **2005**, *23*, 219.
(31) Althorpe, S. C. Semiclassical and Other Methods for Understanding Molecular Collisions and Chemical Reactions In *Collaborative Computational Project on Molecular Quantum Dynamics*; Sen, S., Sokolovski, D., Connor, J. N. L., Eds.; CCP6, Daresbury Laboratory: Warrington, U.K., 2005; pp 58−61. ISBN 0-9545289-3-X.
(32) Panda, A. N.; Althorpe, S. C. *Chem. Phys. Lett.* **2006**, *419*, 245.
(33) Connor, J. N. L.; McCabe, P.; Sokolovski, D.; Schatz, G. C. *Chem. Phys. Lett.* **1993**, *206*, 119.
(34) Sokolovski, D.; Connor, J. N. L.; Schatz, G. C. *Chem. Phys. Lett.* **1995**, *238*, 127.
(35) Sokolovski, D.; Connor, J. N. L.; Schatz, G. C. *J. Chem. Phys.* **1995**, *103*, 5979.
(36) McCabe, P.; Connor, J. N. L. *J. Chem. Phys.* **1996**, *104*, 2297.
(37) Sokolovski, D.; Connor, J. N. L.; Schatz, G. C. *Chem. Phys.* **1996**, *207*, 461.
(38) Wimp, J.; McCabe, P.; Connor, J. N. L. *J. Comput. Appl. Math.* **1997**, *82*, 447.
(39) McCabe, P.; Connor, J. N. L.; Sokolovski, D. *J. Chem. Phys.* **1998**, *108*, 5695.
(40) Sokolovski, D.; Connor, J. N. L. *Chem. Phys. Lett.* **1999**, *305*, 238.
(41) Hollifield, J. J.; Connor, J. N. L. *Phys. Rev. A* **1999**, *59*, 1694.
(42) Hollifield, J. J.; Connor, J. N. L. *Mol. Phys.* **1999**, *97*, 293.
(43) Dobbyn, A. J.; McCabe, P.; Connor, J. N. L.; Castillo, J. F. *Phys. Chem. Chem. Phys.* **1999**, *1*, 1115.
(44) Vrinceanu, D.; Msezane, A. Z.; Bessis, D.; Connor, J. N. L.; Sokolovski, D. *Chem. Phys. Lett.* **2000**, *324*, 311.
(45) McCabe, P.; Connor, J. N. L.; Sokolovski, D. *J. Chem. Phys.* **2001**, *114*, 5194.
(46) Whiteley, T. W. J.; Noli, C.; Connor, J. N. L. *J. Phys. Chem. A* **2001**, *105*, 2792.
(47) Noli, C.; Connor, J. N. L.; Rougeau, N.; Kubach, C. *Phys. Chem. Chem. Phys.* **2001**, *3*, 3946.
(48) Noli, C.; Connor, J. N. L. *Russ. J. Phys. Chem.* **2002**, *76* (Supplement 1), S77. Also available at: http://arXiv.org/abs/physics/0301054.
(49) Anni, R.; Connor, J. N. L.; Noli, C. *Phys. Rev. C* **2002**, *66*, 044610.
(50) Anni, R.; Connor, J. N. L.; Noli, C. *Khim. Fiz.* **2004**, *23* (No 2), 6. Also available at: http://arXiv.org/abs/physics/0410266.
(51) Connor, J. N. L. *Phys. Chem. Chem. Phys.* **2004**, *6*, 377.
(52) Connor, J. N. L.; Anni, R. *Phys. Chem. Chem. Phys.* **2004**, *6*, 3364.
(53) Connor, J. N. L. *Mol. Phys.* **2005**, *103*, 1715.
(54) Xiahou, C.; Connor, J. N. L. Semiclassical and Other Methods for Understanding Molecular Collisions and Chemical Reactions. In *Collaborative Computational Project on Molecular Quantum Dynamics*; Sen, S., Sokolovski, D., Connor, J. N. L., Eds.; CCP6, Daresbury Laboratory: Warrington, U.K., 2005; pp 44−49. ISBN 0-9545289-3-X.
(55) Monks, P. D. D.; Connor, J. N. L.; Althorpe, S. C. Semiclassical and Other Methods for Understanding Molecular Collisions and Chemical Reactions In *Collaborative Computational Project on Molecular Quantum Dynamics*; Sen, S., Sokolovski, D., Connor, J. N. L., Eds.; CCP6, Daresbury Laboratory: Warrington, U.K., 2005; pp 112−118. ISBN 0-9545289-3-X.
(56) Xiahou, C.; Connor, J. N. L. *Mol. Phys.* **2006**, *104*, 159.
(57) Monks, P. D. D.; Xiahou, C.; Connor, J. N. L. *J. Chem. Phys.* **2006**, *125*, 133504.
(58) Schatz, G. C. In *Advances in Classical Trajectory Methods*; Hase, W. L. Ed.; JAI Press: Stamford, CT, 1998; Vol. 3, pp 205−229.
(59) Sokolovski, D. *Russ. J. Phys. Chem.* **2002**, *76* (Supplement 1), S21.
(60) Sokolovski, D.; Castillo, J. F.; Tully, C. *Chem. Phys. Lett.* **1999**, *313*, 225.
(61) Sokolovski, D.; Castillo, J. F. *Phys. Chem. Chem. Phys.* **2000**, *2*, 507.
(62) Sokolovski, D. *Phys. Rev. A* **2000**, *62*, 024702.
(63) Aoiz, F. J.; Bañares, L.; Castillo, J. F.; Sokolovski, D. *J. Chem. Phys.* **2002**, *117*, 2546.
(64) Sokolovski, D. *Chem. Phys. Lett.* **2003**, *370*, 805.
(65) Sokolovski, D.; Msezane, A. Z. *Phys. Rev. A* **2004**, *70*, 032710.
(66) Sokolovski, D.; Sen, S. K.; Aquilanti, V.; Cavalli, S.; De Fazio, D. *J. Chem. Phys.* **2007**, *126*, 084305.
(67) Sokolovski, D.; Msezane, A. Z.; Felfli, Z.; Ovchinnikov, S. Yu.; Macek, J. H. *Nucl. Instrum. Meth. Phys. Res. B* **2007**, *261*, 133.
(68) Sokolovski, D. *Phys. Rev. A* **2007**, *76*, 042125.
(69) Sokolovski, D. *Phys. Scr.* **2007**, *78*, 058118.
(70) Juanes-Marcos, J. C.; Althorpe, S. C.; Wrede, E. *Science* **2005**, *309*, 1227. For a commentary, see: Clary, D. C. *Science* **2005**, *309*, 1195.
(71) Juanes-Marcos, J. C.; Althorpe, S. C.; Wrede, E. *J. Chem. Phys.* **2007**, *126*, 044317.
(72) Panda, A. N.; Althorpe, S. C. *Chem. Phys. Lett.* **2007**, *439*, 50.
(73) Althorpe, S. C.; Juanes-Marcos, J. C.; Wrede, E. *Adv. Chem. Phys.* **2008**, *138*, 1.
(74) Bouakline, F.; Althorpe, S. C.; Ruiz, D. P. *J. Chem. Phys.* **2008**, *128*, 124322.
(75) Guillon, G.; Stoecklin, T. *Euro. Phys. J. D* **2006**, *39*, 359.
(76) Stoecklin, T.; Voronin, A.; Dham, A. K.; Stoker, J. S.-F.; McCourt, F. R. W. *Mol. Phys.* **2008**, *106*, 75.
(77) Fuller, R. C. *Phys. Rev. C* **1975**, *12*, 1561.
(78) Boothroyd, A. I.; Keogh, W. J.; Martin, P. G.; Peterson, M. R. *J. Chem. Phys.* **1996**, *104*, 7139.
(79) Huang, Y.; Zhu, W.; Kouri, D. J.; Hoffman, D. K. *J. Phys. Chem.* **1994**, *98*, 1868.
(80) Dai, D.; Wang, C. C.; Harich, S. A.; Wang, X.; Yang, X.; Chao, S. D.; Skodje, R. T. *Science* **2003**, *300*, 1730.

JP9005586